Spin-Fluctuation-Induced Non-Fermi-Liquid Behavior with Suppressed Superconductivity in $LiFe_{1-x}Co_xAs$

Y. M. Dai,[1] H. Miao,[2] L. Y. Xing,[2] X. C. Wang,[2] P. S. Wang,[3] H. Xiao,[2] T. Qian,[2] P. Richard,[2,4] X. G. Qiu,[2,4] W. Yu,[3,6] C. Q. Jin,[2,4] Z. Wang,[5] P. D. Johnson,[1] C. C. Homes,[1,*] and H. Ding[2,4,†]

[1]*Condensed Matter Physics and Materials Science Department, Brookhaven National Laboratory, Upton, New York 11973, USA*
[2]*Beijing National Laboratory for Condensed Matter Physics, Institute of Physics, Chinese Academy of Sciences, Beijing 100190, China*
[3]*Department of Physics, Renmin University of China, Beijing 100872, China*
[4]*Collaborative Innovation Center of Quantum Matter, Beijing, China*
[5]*Department of Physics, Boston College, Chestnut Hill, Massachusetts 02467, USA*
[6]*Department of Physics and Astronomy, Collaborative Innovation Center of Advanced Microstructures, Shanghai Jiao Tong University, Shanghai 200240, China*

We study a series of $LiFe_{1-x}Co_xAs$ compounds with different Co concentrations by transport, optical spectroscopy, angle-resolved photoemission spectroscopy, and nuclear magnetic resonance. We observe a Fermi-liquid to non-Fermi-liquid to Fermi-liquid (FL-NFL-FL) crossover alongside a monotonic suppression of the superconductivity with increasing Co content. In parallel to the FL-NFL-FL crossover, we find that both the low-energy spin fluctuations and Fermi surface nesting are enhanced and then diminished, strongly suggesting that the NFL behavior in $LiFe_{1-x}Co_xAs$ is induced by low-energy spin fluctuations that are very likely tuned by Fermi surface nesting. Our study reveals a unique phase diagram of $LiFe_{1-x}Co_xAs$ where the region of NFL is moved to the boundary of the superconducting phase, implying that they are probably governed by different mechanisms.

The normal state of high-temperature (high-T_c) superconductors is very unusual, with the electrical resistivity (or quasiparticle scattering rate) varying with temperature in a peculiar way that deviates significantly from the quadratic T dependence expected from Landau's Fermi-liquid (FL) theory of metals [1–4]. Because this anomalous non-Fermi-liquid (NFL) behavior is often revealed experimentally above a superconducting dome, there is a broad consensus that the origin of the NFL behavior may hold the key to understanding the pairing mechanism of high-T_c superconductivity.

Studies on high-T_c cuprate superconductors [1–3], heavy-fermion metals [4,5], organic Bechgaard salts [6], as well as the newly discovered iron-based superconductors (IBSCs) [7–10], have shown that the NFL behavior and high-T_c superconducting dome favor proximity to magnetic order. This fact has led to proposals ascribing both the NFL behavior and high-T_c superconductivity to spin

fluctuations close to a magnetic quantum critical point (QCP) [11–13]. However, a growing number of experiments do not agree with these scenarios. For example, a recent magnetotransport study has shown that by doping $CeCoIn_5$ with Yb, the field-induced QCP is fully suppressed while both the NFL behavior and superconductivity are barely affected [14]. At the current time, the microscopic mechanism of the NFL behavior and its relationship to high-T_c superconductivity are still a matter of considerable debate.

IBSCs feature an intricate phase diagram with NFL behavior, superconducting phase, magnetic order, structural transition, possible QCP(s), and nested Fermi surfaces (FSs) interacting with each other. This complexity makes it quite challenging to distinguish the roles played by different orders or interactions. The $LiFe_{1-x}Co_xAs$ system presents a simple phase diagram: LiFeAs exhibits superconductivity with a maximum transition temperature $T_c \approx 18$ K in its stoichiometric form [15]. The substitution of Fe by Co results in a monotonic lowering of T_c; neither magnetic nor structural transitions have been detected in the temperature-doping (T-x) phase diagram of $LiFe_{1-x}Co_xAs$ [16]. The normal state of LiFeAs is a FL, as evidenced by the quadratic T dependence of the low-temperature resistivity [17,18]. Such a simple phase diagram makes $LiFe_{1-x}Co_xAs$ an excellent system to elucidate

---

the origin of the NFL behavior and its relationship to superconductivity.

In this article, through a combined study of transport, optical spectroscopy, angle-resolved photoemission spectroscopy (ARPES), and NMR on LiFe$_{1-x}$Co$_x$As, we find that while superconductivity is monotonically suppressed with increasing Co concentration, the transport and optical properties reveal a prominent FL-NFL-FL crossover that closely follows the doping evolution of low-energy spin fluctuations (LESFs) and FS nesting. Our observations provide clear evidence that LESFs, which are likely tuned by FS nesting, dominate the normal-state scattering, and are thus responsible for the FL-NFL-FL crossover in LiFe$_{1-x}$Co$_x$As. A unique phase diagram of LiFe$_{1-x}$Co$_x$As derived from our studies shows that the NFL behavior is decoupled from superconductivity, suggesting that they do not share the same origin.

High-quality single crystals of LiFe$_{1-x}$Co$_x$As with different Co concentrations were grown by a self-flux method [15]. Details of the sample synthesis and experimental methods for all the techniques we use in this work are included in Appendixes A–E.

Figures 1(a)–1(e) show the T-dependent resistivity $\rho(T)$ for five representative dopings. For each doping, $\rho(T)$ is fit to a single power law $\rho(T) = \rho_0 + AT^n$, returning the exponent n and the residual resistivity ρ_0. The evolution of n and ρ_0 with doping are summarized in Fig. 1(f) as solid circles and solid diamonds, respectively. In LiFeAs ($x = 0$), $n = 2$, i.e., the resistivity varies quadratically with temperature, indicating a FL normal state, in agreement with previous transport studies on LiFeAs [17,18]. With increasing Co doping, n decreases, reaching a minimum of 1.35 at $x \approx 0.12$. With further doping ($x > 0.12$), n begins to increase and recovers to a value of 2 again at about $x = 0.4$. $\rho(T)$ and the single power-law fitting results for more

dopings are displayed in Appendix B (Fig. 5). To present the crossover behavior more clearly, $\rho(T)$ is plotted as a function of T^n, as shown in Appendix B (Fig. 6), where a linear behavior can be seen for all the dopings. This doping dependence of n is an explicit indication of a doping-induced FL-NFL-FL crossover in LiFe$_{1-x}$Co$_x$As. In addition, we note that, as shown in Fig. 1(f), ρ_0 increases with doping all the way to $x = 0.4$, while n exhibits a FL-NFL-FL crossover in the same doping range. This indicates that the FL-NFL-FL crossover in LiFe$_{1-x}$Co$_x$As is not tied to the impurity level.

Further evidence for the FL-NFL-FL crossover can be revealed by the T dependence of the quasiparticle scattering rate obtained via optical spectroscopy [19,20]. Figure 2(a) displays the real part of the optical conductivity $\sigma_1(\omega)$ for LiFeAs ($x = 0$) at 100 K. The low-frequency $\sigma_1(\omega)$ is dominated by the well-known Drude-like metallic response, where the width of the Drude peak at half maximum gives the value of the quasiparticle scattering rate. In order to accurately extract the quasiparticle scattering rate, we fit the measured $\sigma_1(\omega)$ to the Drude-Lorentz model:

$$\sigma_1(\omega) = \frac{2\pi}{Z_0}\left[\sum_k \frac{\omega_{p,k}^2}{\tau_k(\omega^2 + \tau_k^{-2})} + \sum_j \frac{\gamma_j \omega^2 \Omega_j^2}{(\omega_j^2 - \omega^2)^2 + \gamma_j^2 \omega^2}\right], \quad (1)$$

where $Z_0 \simeq 377\ \Omega$ is the impedance of free space. The first term describes a sum of delocalized (Drude) carrier responses with $\omega_{p,k}$ and $1/\tau_k$ being the plasma frequency and scattering rate in the kth Drude band, respectively. In the second term, ω_j, γ_j, and Ω_j are the resonance frequency, width, and strength of the jth vibration or bound excitation. As shown in Fig. 2(a), the thin red line through the data represents the fitting result for LiFeAs at 100 K, which is
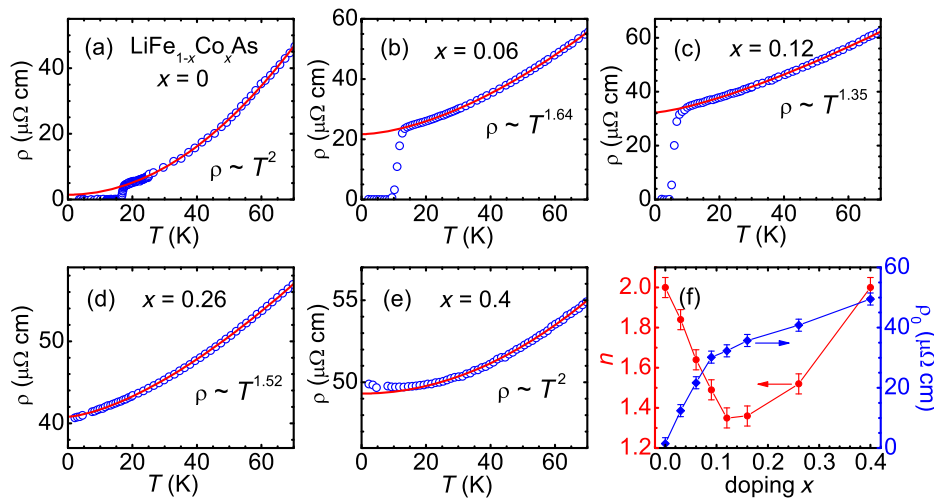

FIG. 1. (a)–(e) Resistivity as a function of temperature $\rho(T)$ (open circles) for LiFe$_{1-x}$Co$_x$As at five selected Co concentrations. For each material, $\rho(T)$ is fit to a single power law $\rho(T) = \rho_0 + AT^n$ (solid lines). (f) Evolution of the exponent n (solid circles) and residual resistivity ρ_0 (solid diamonds) with Co substitution x.
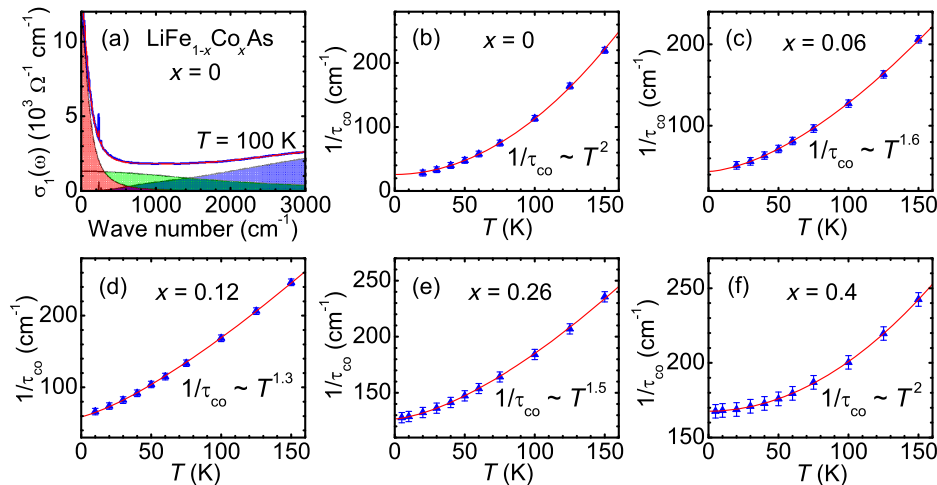
FIG. 2. (a) The thick blue curve is the real part of the optical conductivity $\sigma_1(\omega)$ of LiFeAs ($x = 0$) measured at 100 K. The thin red curve through the data is the Drude-Lorentz fit, which consists of the contributions from a coherent narrow Drude (red shaded region), a nearly incoherent broad Drude (green shaded region), and series of Lorentz components (blue shaded region). (b)–(f) T dependence of the quasiparticle scattering rate $1/\tau_{co}$ derived from the coherent narrow Drude component for five Co concentrations.

decomposed into a coherent narrow Drude, a nearly incoherent broad Drude, and series of Lorentz components, consistent with previous optical studies on IBSCs [19–22]. Fitting results for other dopings at several representative temperatures can be found in Appendix C [Figs. 7(f)–7(j)]. Tu *et al.* suggest that it is more appropriate to describe the broad Drude component as bound excitations [21] because the mean-free path $l = v_F\tau$ (v_F is the Fermi velocity) associated with the broad Drude component is close to the Mott-Ioffe-Regel limit. In any event, since the broad Drude component only gives rise to a T-independent background contribution to the total $\sigma_1(\omega)$, the T dependence of the optical response is governed by the coherent narrow Drude component. As a result, the nature of the broad Drude term does not affect our analysis of the coherent narrow Drude component and the T dependence of $\sigma_1(\omega)$. The application of the Drude-Lorentz analysis at all the measured temperatures for five representative dopings yields the T dependence of the scattering rate of the coherent narrow Drude component $1/\tau_{co}$, shown in Figs. 2(b)–2(f). For each doping, $1/\tau_{co}$ follows the expression $1/\tau_{co} = 1/\tau_0 + BT^\alpha$ with the exponent $\alpha \approx n$, where n is the exponent determined from the fit to $\rho(T)$ for the corresponding dopings. Again, we plot $1/\tau_{co}$ as a function of T^α in Appendix C [Figs. 7(k)–7(o)], which reveals distinct linear behavior for all the dopings. Such crossover behavior of α provides further evidence for the doping-induced FL-NFL-FL changes in LiFe$_{1-x}$Co$_x$As.

In order to gain insight into the origin of the anomalous FL-NFL-FL crossover in LiFe$_{1-x}$Co$_x$As, we examine the evolution of LESFs with Co concentration by looking into the nuclear spin-lattice relaxation rate $1/T_1T$, reflecting the summation of all different **q** modes of sub-meV LESFs weighted by a nearly uniform form factor, which

can be determined from ^{75}As NMR measurements [8,23]. Figure 3(l) displays the T dependence of $1/T_1T$ for five different dopings. In LiFeAs ($x = 0$), $1/T_1T$ is almost T independent, and a negligible upturn at low temperature indicates weak LESFs. However, in sharp contrast to LiFeAs, $1/T_1T$ for $x = 0.12$ increases rapidly upon cooling and a prominent upturn develops at low temperature, implying that LESFs are significantly enhanced. For $x = 0.26$, the upturn in $1/T_1T$ at low temperature becomes less prominent, suggesting that the LESFs diminish again. The low-temperature upturn in $1/T_1T$ can be empirically described by the Curie-Weiss expression $1/T_1T = A + BT + C/(T + \theta)$ [solid lines in Fig. 3(l)], in good agreement with previous NMR studies [8,23]. To quantify the doping dependence of the LESFs, we take the value of $1/T_1T$ at 20 K (just above T_c of LiFeAs), $1/T_1T|_{T=20\,K}$, for each doping and plot them as a function of x [solid squares in Fig. 3(m)]. Upon doping, $1/T_1T|_{T=20\,K}$ first grows but then drops, resulting in a peak at $x = 0.12$. The link between the LESFs and the NFL behavior can be revealed by comparing the doping dependence of n [solid circles in Fig. 1(f)] and $1/T_1T|_{T=20\,K}$ [solid squares in Fig. 3(m)]. Below $x = 0.12$, the enhancement of LESFs (increase in $1/T_1T|_{T=20\,K}$) leads to a more conspicuous deviation from a FL (decrease in n) while above $x = 0.12$, the reduction of LESFs (decrease in $1/T_1T|_{T=20\,K}$) results in a gradual recovery of the FL behavior (increase in n). The most robust NFL behavior ($n \approx 1.35$) occurs at $x = 0.12$ where the LESFs are optimized ($1/T_1T|_{T=20\,K}$ peaks). These observations strongly suggest that the FL-NFL-FL crossover in LiFe$_{1-x}$Co$_x$As is governed by LESFs.

Since an investigation into the FS may provide information on the nature of the LESFs, we then study the evolution of the FSs in LiFe$_{1-x}$Co$_x$As. The FS contour of
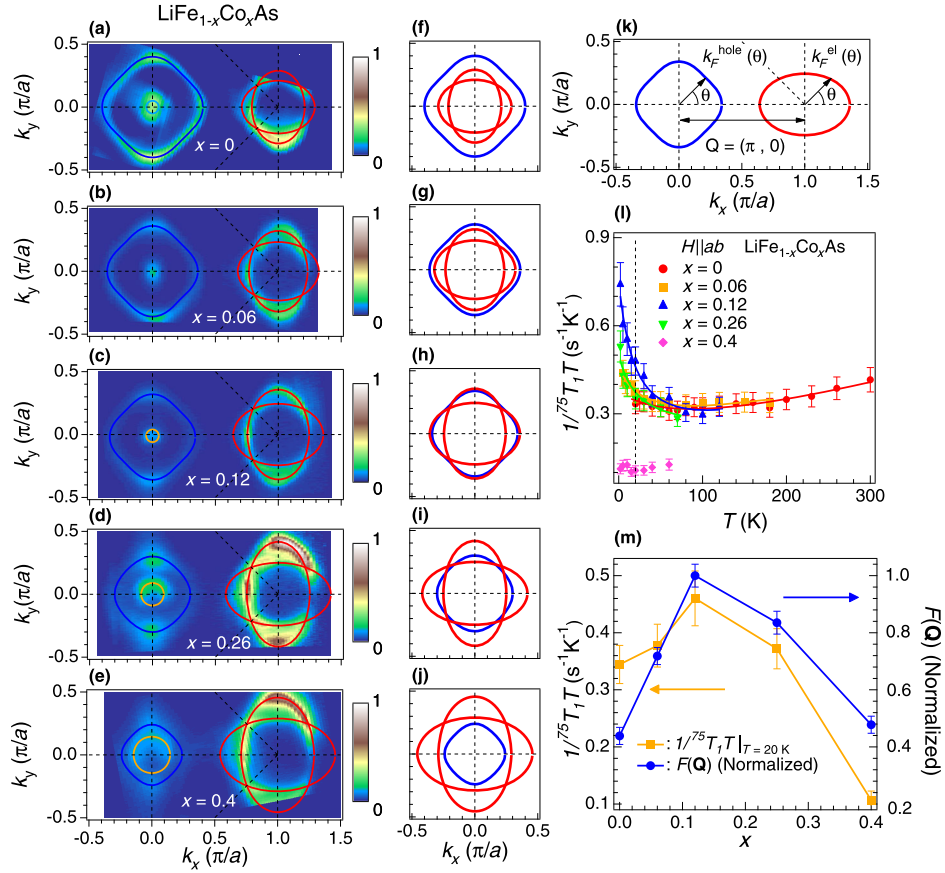
FIG. 3.   (a)–(e) FS contour of LiFe$_{1-x}$Co$_x$As for five representative Co concentrations, determined by integrating the ARPES spectral intensity within ± 10 meV with respect to E_F. (f)–(j) Extracted FSs from corresponding ARPES measurements for each doping. (k) Definition of $\mathbf{k}_\mathbf{F}^{\text{hole}}(\theta)$, $\mathbf{k}_\mathbf{F}^{\text{el}}(\theta)$, and $\mathbf{Q}$ in the k space. (l) Spin-lattice relaxation rate ^{75}As $1/T_1T$ as a function of temperature for five Co concentrations measured by NMR. (m) Evolution of ^{75}As $1/T_1T$ at 20 K (solid squares) and FS nesting factor (solid circles) with increasing Co concentration.

LiFe$_{1-x}$Co$_x$As is traced out from the ARPES intensity plot near the Fermi energy (E_F) for five representative dopings [Figs. 3(a)–3(e)]. The extracted FSs for each doping are shown in Figs. 3(f)–3(j). For LiFeAs ($x = 0$), two hole and two electron FS pockets are observed at the Γ and M points, respectively [Fig. 3(a)], in accord with previous ARPES studies [24,25]. The inner hole pocket is quite small, while the outer hole pocket is much larger than the electron pockets, resulting in a poor nesting condition in LiFeAs [Fig. 3(f)]. With Co doping, the electron pockets expand while the hole pockets shrink. Consequently, the FS nesting is improved. As shown in Fig. 3(h), the shape of the hole FS matches the outer contour of the two electron FSs at $x \approx 0.12$. Further Co doping ($x > 0.12$) makes the electron and hole pockets mismatched again, e.g., $x = 0.4$ [Figs. 3(e) and 3(j)], leading to a degradation of the FS nesting. In order to quantitatively analyze the FS nesting, we define a nesting factor at vector $\mathbf{Q}$,

$$F(\mathbf{Q}) = \sum_{i,j} \int_0^{2\pi} \frac{1}{\|\mathbf{k}_\mathbf{F}^{\text{el}_i}(\theta) - \mathbf{k}_\mathbf{F}^{\text{hole}_j}(\theta) - \mathbf{Q}\| + \delta}\, d\theta, \quad (2)$$

where the definitions of $\mathbf{k}_\mathbf{F}^{\text{el}}(\theta)$, $\mathbf{k}_\mathbf{F}^{\text{hole}}(\theta)$, and $\mathbf{Q}$ are illustrated in Fig. 3(k); δ is a small positive number to avoid singular behavior; for an n-dimensional vector $\mathbf{x}$, $\|\mathbf{x}\| = \sqrt{\mathbf{x} \cdot \mathbf{x}} = \sqrt{\sum_{i=1}^n (x_i)^2}$. $F(\mathbf{Q})$ increases as the FS nesting is improved, and is maximized when the hole FS matches the outer contour of the two electron FSs. Assuming v_F is uniform on all FSs, the nesting factor $F(\mathbf{Q})$ is proportional to the noninteracting single-orbital magnetic susceptibility at vector $\mathbf{Q}$:

$$\chi^{(0)}(\mathbf{Q}) = \sum_\mathbf{p} \frac{f_\mathbf{p} - f_{\mathbf{p}+\mathbf{Q}}}{\varepsilon_{\mathbf{p}+\mathbf{Q}} - \varepsilon_\mathbf{p}}, \quad (3)$$

where $f_\mathbf{p}$ is the Fermi distribution and $\varepsilon_\mathbf{p}$ is the quasiparticle kinetic energy. $F(\mathbf{Q})$ is calculated by Eq. (2) for each doping and normalized by its value at $x = 0.12$. All FSs have been considered in the calculation. The solid circles in Fig. 3(m) portray the doping dependence of $F(\mathbf{Q})$. Remarkably, $F(\mathbf{Q})$ follows exactly the same doping dependence as $1/T_1T|_{T=20\text{ K}}$, indicating that the LESFs probed by NMR are closely related to the FS nesting. The

FS structure naturally suggests that the spin fluctuations are of the antiferromagnetic type with large wave vectors close to the nesting vectors $(\pm\pi, 0)$ and $(0, \pm\pi)$. This is indeed consistent with our NMR data. The Knight shift that measures the uniform susceptibility becomes T independent below 30 K (Appendix E, Fig. 11), indicating that the low-temperature upturn in $1/T_1 T$ comes from large-momentum spin fluctuations. Note that since the NMR form factor for As is known to be broadly distributed in momentum space in IBSCs [27], both commensurate (close to FS nesting) and incommensurate (away from nesting) LESFs are captured by the spin-lattice relaxation rate $1/T_1 T$.

In Fig. 4, we summarize our experimental results in the T-x phase diagram of $LiFe_{1-x}Co_xAs$. With increasing Co concentration x that monotonically suppresses the superconducting transition temperature T_c by electron doping, we observe the following. (i) The T dependence of the resistivity $\rho(T) \propto AT^n$ and the optical scattering rate
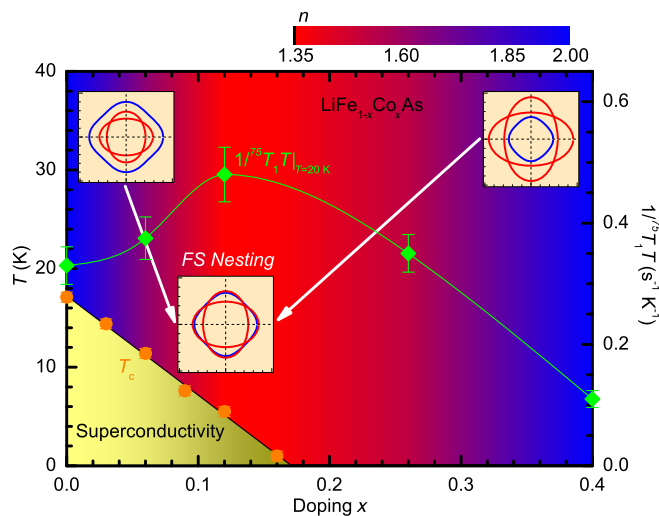

FIG. 4. Temperature-doping $(T$-$x)$ phase diagram of $LiFe_{1-x}Co_xAs$. Superconductivity (yellow regime) is monotonically suppressed with increasing Co concentration x and terminates at a critical value $x \approx 0.17$. The normal state of LiFeAs is a Fermi liquid (blue regime at $x = 0$), where the T-dependent resistivity follows $\rho(T) = \rho_0 + AT^n$, with $n = 2$. A crossover from Fermi liquid to non-Fermi liquid is induced by Co doping. At $x = 0.12$, n reaches its minimum value of 1.35, indicating the most robust non-Fermi-liquid behavior (red regime). Further doping results in a reversal of this trend until by $x = 0.4$ the Fermi-liquid behavior is fully recovered (blue regime at $x = 0.4$). The green diamonds denote the spin-lattice relaxation rate at 20 K $(1/T_1 T|_{T=20 \text{ K}})$ measured by NMR for several representative dopings. $1/T_1 T|_{T=20 \text{ K}}$ reaches the maximum at $x \approx 0.12$, signifying that low-energy spin fluctuations are optimized at this doping. The three inset panels depict the extracted Fermi surfaces for three representative Co concentrations: $x = 0$ (left), $x = 0.12$ (middle), and $x = 0.4$ (right). While the Fermi surface nesting is poor for $x = 0$ and 0.4, the nesting condition is significantly improved at $x = 0.12$.

$1/\tau(T) \propto BT^\alpha$ deviates from a FL $(n, \alpha = 2)$ observed near $x = 0$, reaching the most pronounced NFL power-law behavior $(n \simeq \alpha \simeq 1.35)$ at $x \simeq 0.12$ and then gradually returns for $x > 0.12$ to the FL values at $x = 0.4$. (ii) The NMR spin-lattice relaxation rate $1/T_1 T$ shows that LESFs, small at $x = 0$, gradually enhance and become strongest at $x = 0.12$, but diminish for $x > 0.12$. (iii) ARPES measurements reveal that while the electron and hole FS pockets are far from being nested at $x = 0$, the nesting improves with doping, is optimized near $x = 0.12$, and then degrades with further electron doping for $x > 0.12$. (iv) No long-range magnetic order is observed in the T-x phase diagram of $LiFe_{1-x}Co_xAs$ up to $x = 0.4$, which is consistent with previous studies [15,16,28,29].

A comparison between observations (i) and (ii) strongly suggests that the FL-NFL-FL crossover in $LiFe_{1-x}Co_xAs$ is induced by LESFs. Point (iii) in combination with (i) and (ii) implies that the integrated LESFs probed by NMR are dominated by, or at least scale with, those near $\mathbf{q} \sim \mathbf{Q}$, which are most likely tuned by FS nesting. The fact (iv) does not directly support a magnetic QCP in the T-x phase diagram of $LiFe_{1-x}Co_xAs$. However, the pronounced NFL behavior observed near $x = 0.12$, which is usually considered as a signature of quantum criticality [2,5,13], in conjunction with the strong tendency to diverge in $1/T_1 T$ upon cooling at the same doping, points to an incipient QCP near $x = 0.12$. A magnetic order may emerge under pressure or magnetic field in the material with $x = 0.12$, resulting in an actual magnetic QCP associated with other tuning parameters. Finally, the NFL behavior is observed at the boundary of the superconducting phase, implying that they are likely to be governed by different mechanisms.

APPENDIX A: SAMPLE SYNTHESIS AND CHARACTERIZATION

1. Sample synthesis

High-quality single crystals of LiFe$_{1-x}$Co$_x$As are grown with the self-flux method. The precursor of Li$_3$As is prepared by sintering Li foil and an As lump at about 700 °C for 10 h in a Ti tube filled with Ar atmosphere. Fe$_{1-x}$Co$_x$As is prepared by mixing the Fe, Co, and As powders thoroughly, and then sealed in an evacuated quartz tube, and sintered at 700 °C for 30 h. To ensure the homogeneity of the product, these pellets are reground and heated for a second time. The Li$_3$As, Fe$_{1-x}$Co$_x$As, and As powders are mixed according to the elemental ratio Li(Fe$_{1-x}$Co$_x$)$_{0.3}$As. The mixture is put into an alumina oxide tube and subsequently sealed in a Nb tube and placed in a quartz tube under vacuum. The sample is heated at 650 °C for 10 h and then heated up to 1000 °C for another 10 h. Finally, it is cooled down to 750 °C at a rate of 2 °C per hour. Crystals with a size up to 5 mm are obtained. The entire process of preparing the starting materials and the evaluation of the final products are carried out in a glovebox purged with high-purity Ar gas.

2. Determination of the doping level

The molar ratio of Co and Fe of the LiFe$_{1-x}$Co$_x$As single crystals is checked by energy-dispersive x-ray spectroscopy (EDS) at several points on one or two selected samples for each Co concentration. For each doping, the Co concentration measured by EDS is consistent with the nominal value.

APPENDIX B: TRANSPORT

1. Resistivity measurements

The electrical transport measurements of LiFe$_{1-x}$Co$_x$As are carried out in a commercial physical properties

measurement system (PPMS) using the four-probe method. To prevent sample degradation, the electrical contacts are prepared in a glovebox and then the sample is protected by *n* grease before transferring to the PPMS. Each sample is cut into a rectangular piece, so that its dimensions can be measured more accurately with a microscope. With these precisely measured geometry factors, the resistivity can be easily calculated from the measured resistance. The resistivity determined from the transport measurements is then compared with the values determined from the optical conductivity to ensure the consistency between different techniques.

2. Single power-law fitting

Figure 5 displays the resistivity as a function of temperature $\rho(T)$ (open circles) up to 70 K for all 8 samples. For each substitution, $\rho(T)$ is fit to a single power-law expression, $\rho(T) = \rho_0 + AT^n$, from ~2 K (or T_c, whichever is greater) up to 70 K. The solid lines through the data in each panel denote the fitting results. The power n, determined from the fitting, is shown for the stoichiometric material and all the Co substitutions in the corresponding panels; the crossover behavior of n can be seen clearly.

In order to present the power-law behavior of the $\rho(T)$ curve more clearly, we plot $\rho(T)$ as a function of T^n for each substitution in Fig. 6, where n is the power determined from the single power-law fitting. In this case, all the $\rho(T)$ curves can be perfectly described by linear behavior, shown by the solid line in each panel.

APPENDIX C: OPTICAL SPECTROSCOPY

1. Reflectivity

The temperature dependence of the absolute reflectivity $R(\omega)$ of LiFe$_{1-x}$Co$_x$As is measured at a near-normal

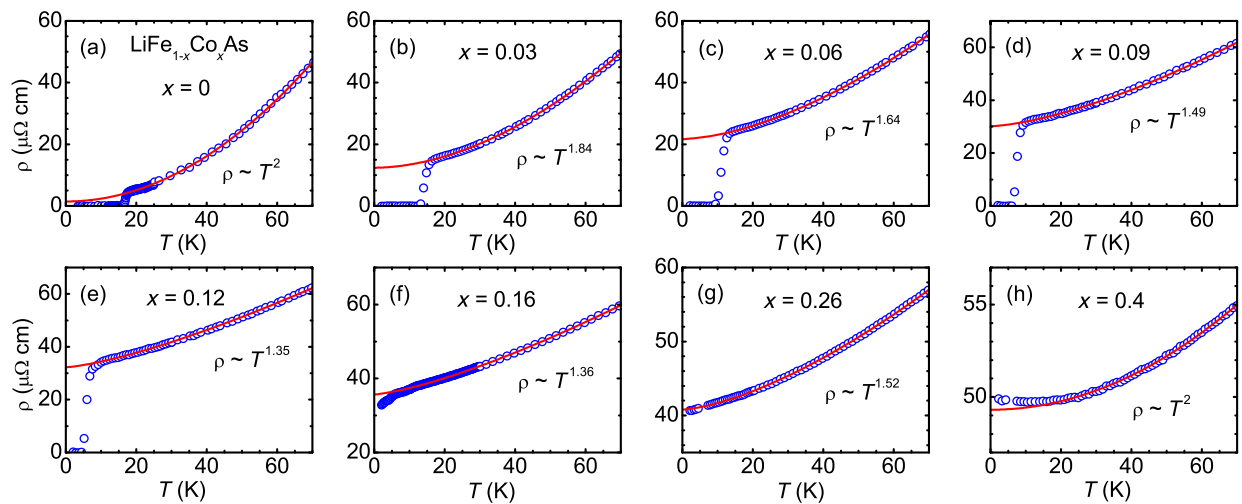FIG. 5.   (a)–(h) Resistivity of LiFe$_{1-x}$Co$_x$As as a function of temperature for different Co values. For each sample, the resistivity curve is fit to the single power-law expression $\rho(T) = \rho_0 + AT^n$. The open circles denote the measured resistivity and the solid lines in each panel are the fitting results. The power n derived from the fitting is shown in each panel.
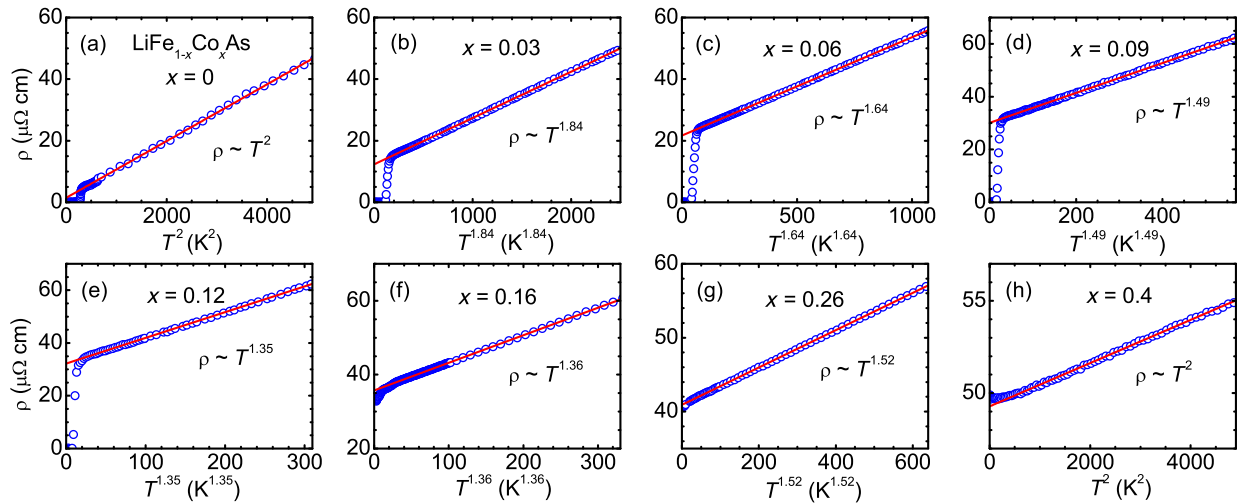
FIG. 6.   (a)–(h) Resistivity of LiFe$_{1-x}$Co$_x$As as a function of T^n for different Co values. n is the power determined from the single power-law fit to the resistivity as a function of T. The straight solid line in each panel is a guide to the eye.

angle of incidence for the stoichiometric material and 4 representative substitutions using an *in situ* overcoating technique [30]. For each sample, data are collected at 17 different temperatures from 5 K to room temperature over a wide frequency range (∼2 meV–4 eV) on a freshly cleaved surface. Because of the air-sensitive nature of the LiFe$_{1-x}$Co$_x$As samples, the sample mounting and cleaving are done in a glove bag purged with high-purity Ar gas. Immediately after the cleaving, the sample is transferred to the vacuum shroud (also purged with Ar) with the protection of a small Ar-purged plastic bag. The reproducibility of the experimental results is checked by repeating the $R(\omega)$ measurements 2 or 3 times for each doping. Figures 7(a)–7(e) show $R(\omega)$ in the far-infrared region at 4 selected temperatures for 5 different Co concentrations. For all the materials, $R(\omega)$ approaches unity at zero frequency and increases upon cooling, indicating a metallic response.

2. Kramers-Kronig analysis

The real part of the complex optical conductivity $\sigma_1(\omega)$ is determined from a Kramers-Kronig analysis of the reflectivity. Given the metallic nature of the LiFe$_{1-x}$Co$_x$As materials, the Hagen-Rubens form $[R(\omega) = 1 - A\sqrt{\omega}]$ is used for the low-frequency extrapolation, where A is chosen to match the data at the lowest measured frequency. Above the highest measured frequency, $R(\omega)$ is assumed to be constant up to 1.0×10^5 cm^{-1}, above which a free-electron response $[R(\omega) \propto \omega^{-4}]$ is used.

3. Optical conductivity

Figures 7(f)–7(j) display $\sigma_1(\omega)$ at 4 selected temperatures for the stoichiometric material and 4 different Co concentrations. The metallic behavior of these materials

can be recognized by the pronounced Drude-like peak centered at zero frequency. The zero-frequency value of $\sigma_1(\omega)$ represents the dc conductivity σ_{dc}, which is in good agreement with the values determined from transport measurements; the width of the Drude peak at half maximum yields the quasiparticle scattering rate. As the temperature decreases, σ_{dc} increases and the Drude peak narrows. This indicates that the quasiparticle scattering rate decreases upon cooling, dominating the temperature dependence of the electrical transport properties.

4. Quasiparticle scattering rate

Figures 7(k)–7(o) show the quasiparticle scattering rate of the coherent narrow Drude component $1/\tau_{co}$ as a function of T^α, where α is the power determined from the single power-law fit to $1/\tau_{co}$ as a function of T. Linear behavior can be clearly observed in each panel as guided by the straight solid lines.

5. Comparison between transport and optics

Figure 8(a) compares the doping dependence of ρ_0 (solid circles) and $1/\tau_0$ (solid triangles), where ρ_0 is determined by fitting $\rho(T)$ to $\rho(T) = \rho_0 + AT^n$, and $1/\tau_0$ is derived by fitting $1/\tau_{co}(T)$ to $1/\tau_{co}(T) = 1/\tau_0 + BT^\alpha$ for each doping. Both ρ_0 and $1/\tau_0$ grow as the Co concentration increases, indicating that impurities are introduced into the compounds by the Co substitution. The single power-law fit also returns the coefficients A for transport and B for optics, respectively. As shown in Fig. 8(b), A (solid circles) and B (solid triangles) follow identical doping dependence, suggesting that the T dependence in $\rho(T)$ and $1/\tau_{co}(T)$ is governed by the same physics. Note that while the coefficients A and B follow exactly the same trace across doping, the detailed behaviors of ρ_0 and $1/\tau_0$ are slightly
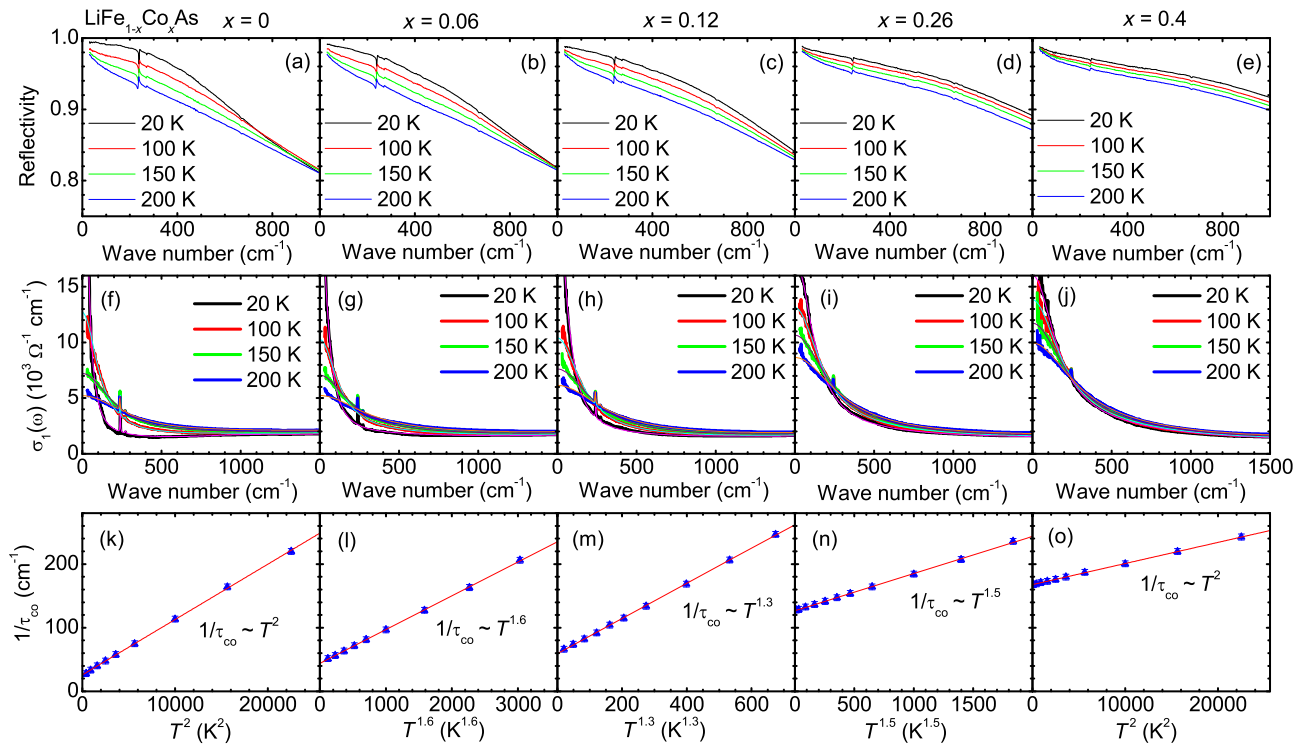
FIG. 7.   Reflectivity, optical conductivity, and quasiparticle scattering rate of $LiFe_{1-x}Co_xAs$. (a)–(e) Temperature dependence of the reflectivity of $LiFe_{1-x}Co_xAs$ in the far-infrared region at several temperatures for the stoichiometric material and 4 representative Co concentrations. (f)–(j) Real part of the optical conductivity derived from the reflectivity. The thick solid curves are the experimental data and the thin solid curves through the data denote the Drude-Lorentz fitting results. (k)–(o) Scattering rate of the coherent narrow Drude component ($1/\tau_{co}$) as a function of T^α. The straight solid line in each panel is a guide to the eye.
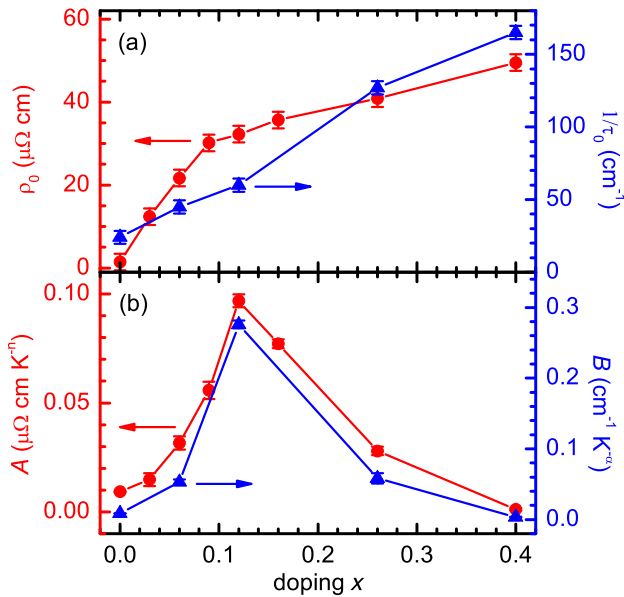

FIG. 8.   (a) Doping dependence of ρ_0 (solid circles) and $1/\tau_0$ (solid triangles). (b) Coefficients A for transport (solid circles) and B for optics (solid triangles) determined from the single power-law fit as a function of Co concentration.

different. This is because $1/\tau_0$ is the residual scattering rate of the coherent narrow Drude component, which contributes to ρ_0 in parallel with the incoherent broad Drude component. However, as a common feature in all Fe-based superconductors [19,20], the T dependence of the transport properties is dominated by the coherent narrow Drude component. Since A and B are the prefactors that describe the properties of the T dependence in $\rho(T)$ and $1/\tau_{co}(T)$, respectively, it is natural to expect similar behaviors for A and B if they are governed by the same physics.

APPENDIX D: ANGLE-RESOLVED PHOTOEMISSION SPECTROSCOPY

1. Measurements

ARPES measurements are performed with a high-flux He discharge lamp. The energy resolution is set at 12 and 3 meV for the Fermi surface mapping and high-resolution measurements, respectively. The angular resolution is set at 0.2°. Fresh surfaces for the ARPES measurements are obtained by an *in situ* cleavage of the crystals in a working vacuum better than 4×10^{-11} Torr. The Fermi energy (E_F) of the samples is referenced to that of a gold film evaporated onto the sample holder.

2. ARPES intensity plots and energy and momentum distribution curves along the Γ-M direction

ARPES intensity plots across the Γ point for five representative dopings and their corresponding energy distribution curves (EDCs) are shown in Figs. 9(a)–9(e) and Figs. 9(f)–9(j), respectively. The same plots but crossing the M point for each doping are shown in Figs. 9(k)–9(o) and Figs. 9(p)–9(t), respectively. The red curves in Figs. 9(a)–9(e) and Figs. 9(k)–9(o) are the momentum distribution curves (MDCs) at the Fermi

level. The peak positions on MDCs correspond to the k_F positions along the high-symmetry line. Since the EDC and MDC peaks, as well as the band dispersions, are well defined at all dopings, the k_F positions can be accurately determined for each Co concentration. The uncertainty of the k_F position is mainly from the energy and momentum resolutions of our system settings. For these measurements the angular and energy resolutions of the system are set at $0.2°$ and 3 meV, respectively, which lead to a typical uncertainty of $\pm 0.01\pi/a$ for k_F at 21.2 eV photon energy.
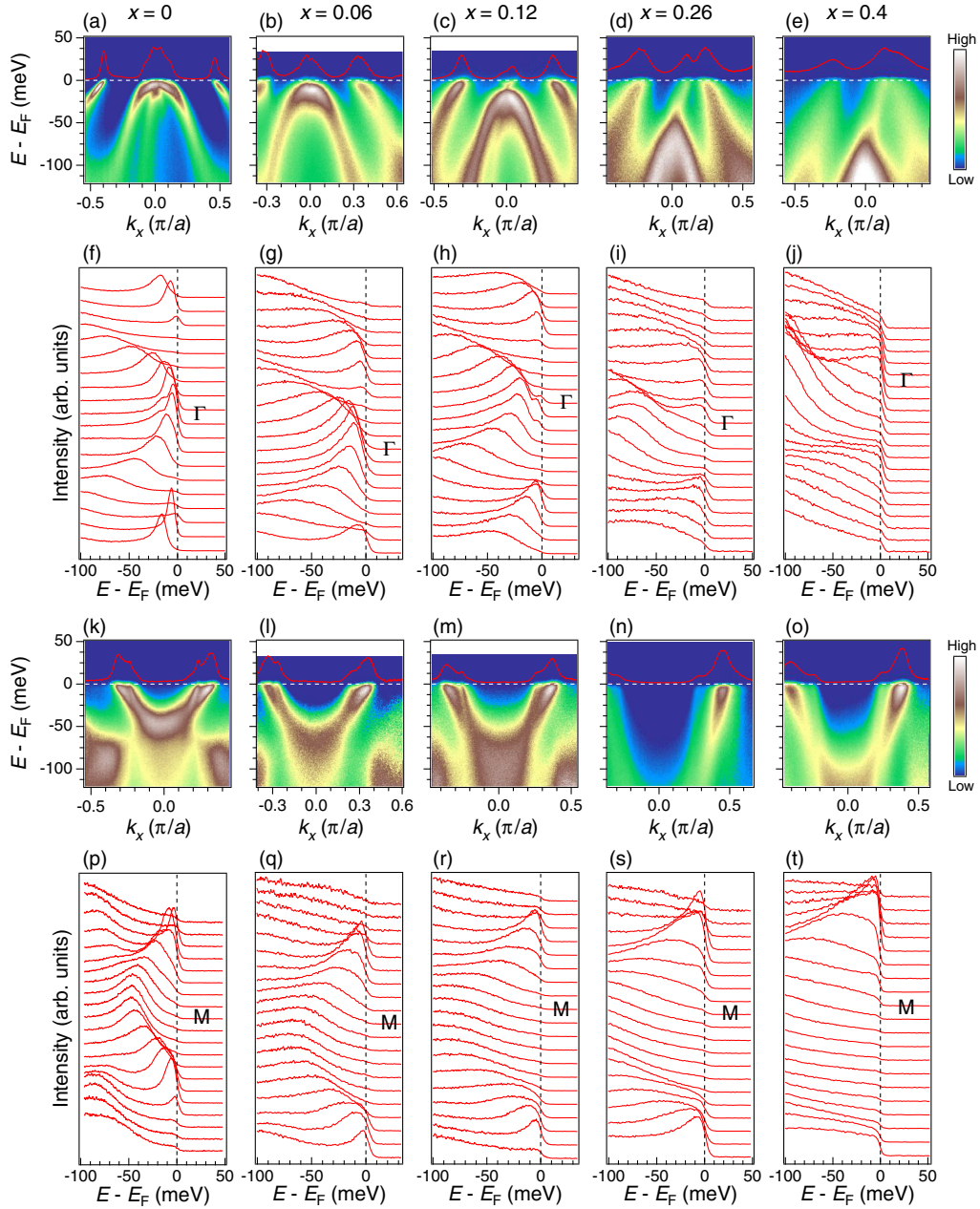

FIG. 9.   (a)–(j) ARPES intensity plots and corresponding EDCs at the Brillouin zone center. (k)–(t) ARPES intensity plots and corresponding EDCs at the M point. All data are taken at 20 K along the Γ-M direction. The red curves shown in the intensity plots are MDCs at the Fermi level.
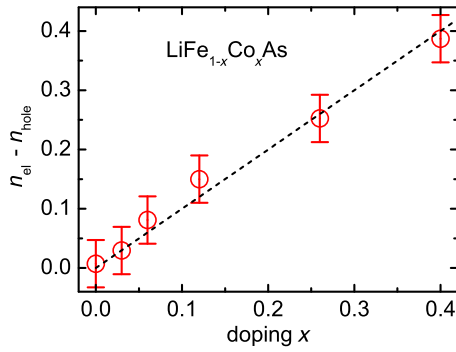
FIG. 10.   Total electronic carrier concentration (open circles) determined from the total algebraic Fermi surface volume at each Co concentration x. The dashed line corresponds to the carrier concentration assumed by adding one extra electron for each Fe substituted by Co.

3. Evolution of the Fermi surface volume with doping

The evolution of the Fermi surface volume with doping is controlled by the Luttinger theorem: the total algebraic Fermi surface volume is directly proportional to the carrier concentration. We check that this is the case in our study and we plot the results in Fig. 10, which confirm that the total volume of the Fermi surface (open circles) satisfies the Luttinger theorem at each doping if we assume a rigid chemical potential shift caused by the introduction of one additional electron carrier per Fe atom substituted by Co (dashed line), as also observed theoretically [31] and experimentally [32,33] for the 122 family of iron pnictides.

APPENDIX E: NUCLEAR MAGNETIC RESONANCE

1. Measurements

We perform the ^{75}As NMR measurements with the external field parallel to the a-b plane. The spin-lattice relaxation rate is measured by the inversion-recovery method on the central transition, and the recovery curve is fit with a standard double exponential form for an $S = 3/2$ spin:

$$1 - \frac{m(t)}{m(0)} = 0.9 \exp\left(\frac{-6t}{T_1}\right) + 0.1 \exp\left(\frac{-t}{T_1}\right). \quad \text{(E1)}$$

2. Knight shift

Figure 11 shows the Knight shifts of $x = 0$ and $x = 0.12$ samples, respectively. The Knight shift, which measures the uniform susceptibility, becomes temperature independent below 30 K, indicating that the low-temperature upturn in $1/T_1 T$ comes from large-momentum spin fluctuations. Note that since the NMR form factor for As is known to be broadly distributed in momentum space in iron-based
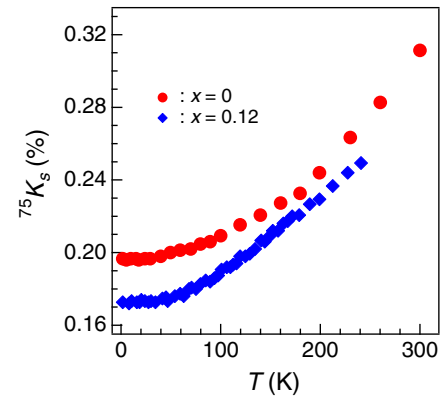

FIG. 11.   The Knight shifts of LiFe$_{1-x}$Co$_x$As for the $x = 0$ and $x = 0.12$ samples. The Knight shift for both samples is measured with the external field perpendicular to the a-b plane to avoid calculation of the second-order quadruple correction. Though the size of the Knight shift along different directions may be different, they share the same temperature dependence. Therefore, we are able to take the K_s at $H\|c$ to estimate the behavior of $H\|ab$ [26].

superconductors [27], both commensurate (close to FS nesting) and incommensurate (away from nesting) low-energy spin fluctuations are captured by the spin-lattice relaxation rate $1/T_1 T$.

[1] G. S. Boebinger, *An Abnormal Normal State*, Science **323,** 590 (2009).

[2] R. A. Cooper, Y. Wang, B. Vignolle, O. J. Lipscombe, S. M. Hayden, Y. Tanabe, T. Adachi, Y. Koike, M. Nohara, H. Takagi *et al.*, *Anomalous Criticality in the Electrical Resistivity of* La$_{2-x}$Sr$_x$CuO$_4$, Science **323,** 603 (2009).

[3] K. Jin, N. P. Butch, K. Kirshenbaum, J. Paglione, and R. L. Greene, *Link between Spin Fluctuations and Electron Pairing in Copper Oxide Superconductors*, Nature (London) **476,** 73 (2011).

[4] H. v. Löhneysen, A. Rosch, M. Vojta, and P. Wölfle, *Fermi-Liquid Instabilities at Magnetic Quantum Phase Transitions*, Rev. Mod. Phys. **79,** 1015 (2007).

[5] P. Gegenwart, Q. Si, and F. Steglich, *Quantum Criticality in Heavy-Fermion Metals*, Nat. Phys. **4,** 186 (2008).

[6] N. Doiron-Leyraud, P. Auban-Senzier, S. René de Cotret, C. Bourbonnais, D. Jérome, K. Bechgaard, and L. Taillefer, *Correlation between Linear Resistivity and T_c in the Bechgaard Salts and the Pnictide Superconductor* Ba(Fe$_{1-x}$Co$_x$)$_2$As$_2$, Phys. Rev. B **80,** 214531 (2009).

[7] K. Hashimoto, K. Cho, T. Shibauchi, S. Kasahara, Y. Mizukami, R. Katsumata, Y. Tsuruhara, T. Terashima, H. Ikeda, M. A. Tanatar *et al.*, *A Sharp Peak of the Zero-Temperature Penetration Depth at Optimal Composition in* BaFe$_2$(As$_{1-x}$P$_x$)$_2$, Science **336,** 1554 (2012).

[8] R. Zhou, Z. Li, J. Yang, D. L. Sun, C. T. Lin, and G.-Q. Zheng, *Quantum Criticality in Electron-Doped* BaFe$_{2-x}$Ni$_x$As$_2$, Nat. Commun. **4,** 2265 (2013).

[9] J. G. Analytis, H.-H. Kuo, R. D. McDonald, M. Wartenbe, P. M. C. Rourke, N. E. Hussey, and I. R. Fisher, *Transport*

Near a Quantum Critical Point in $BaFe_2(As_{1-x}P_x)_2$, Nat. Phys. **10**, 194 (2014).

[10] T. Shibauchi, A. Carrington, and Y. Matsuda, *A Quantum Critical Point Lying Beneath the Superconducting Dome in Iron Pnictides*, Annu. Rev. Condens. Matter Phys. **5**, 113 (2014).

[11] T. Moriya and K. Ueda, *Spin Fluctuations and High Temperature Superconductivity*, Adv. Phys. **49**, 555 (2000).

[12] L. Taillefer, *Scattering and Pairing in Cuprate Superconductors*, Annu. Rev. Condens. Matter Phys. **1**, 51 (2010).

[13] S. Sachdev and B. Keimer, *Quantum Criticality*, Phys. Today **64**, No. 2, 29 (2011).

[14] T. Hu, Y. P. Singh, L. Shu, M. Janoschek, M. Dzero, M. B. Maple, and C. C. Almasan, *Non-Fermi Liquid Regimes with and without Quantum Criticality in* $Ce_{1-x}Yb_xCoIn_5$, Proc. Natl. Acad. Sci. U.S.A. **110**, 7160 (2013).

[15] X. Wang, Q. Liu, Y. Lv, W. Gao, L. Yang, R. Yu, F. Li, and C. Jin, *The Superconductivity at 18 K in LiFeAs System*, Solid State Commun. **148**, 538 (2008).

[16] M. J. Pitcher, T. Lancaster, J. D. Wright, I. Franke, A. J. Steele, P. J. Baker, F. L. Pratt, W. T. Thomas, D. R. Parker, S. J. Blundell *et al.*, *Compositional Control of the Superconducting Properties of LiFeAs*, J. Am. Chem. Soc. **132**, 10467 (2010).

[17] O. Heyer, T. Lorenz, V. B. Zabolotnyy, D. V. Evtushinsky, S. V. Borisenko, I. Morozov, L. Harnagea, S. Wurmehl, C. Hess, and B. Büchner, *Resistivity and Hall Effect of LiFeAs: Evidence for Electron-Electron Scattering*, Phys. Rev. B **84**, 064512 (2011).

[18] F. Rullier-Albenque, D. Colson, A. Forget, and H. Alloul, *Multiorbital Effects on the Transport and the Superconducting Fluctuations in LiFeAs*, Phys. Rev. Lett. **109**, 187005 (2012).

[19] D. Wu, N. Barišić, P. Kallina, A. Faridian, B. Gorshunov, N. Drichko, L. J. Li, X. Lin, G. H. Cao, Z. A. Xu *et al.*, *Optical Investigations of the Normal and Superconducting States Reveal Two Electronic Subsystems in Iron Pnictides*, Phys. Rev. B **81**, 100512 (2010).

[20] Y. M. Dai, B. Xu, B. Shen, H. Xiao, H. H. Wen, X. G. Qiu, C. C. Homes, and R. P. S. M. Lobo, *Hidden T-Linear Scattering Rate in* $Ba_{0.6}K_{0.4}Fe_2As_2$ *Revealed by Optical Spectroscopy*, Phys. Rev. Lett. **111**, 117001 (2013).

[21] J. J. Tu, J. Li, W. Liu, A. Punnoose, Y. Gong, Y. H. Ren, L. J. Li, G. H. Cao, Z. A. Xu, and C. C. Homes, *Optical Properties of the Iron Arsenic Superconductor* $BaFe_{1.85}Co_{0.15}As_2$, Phys. Rev. B **82**, 174509 (2010).

[22] M. Nakajima, S. Ishida, T. Tanaka, K. Kihou, Y. Tomioka, T. Saito, C. H. Lee, H. Fukazawa, Y. Kohori, T. Kakeshita *et al.*, *Normal-State Charge Dynamics in Doped* $BaFe_2As_2$: *Roles of Doping and Necessary Ingredients for Superconductivity*, Sci. Rep. **4**, 5873 (2014).

[23] Y. Nakai, T. Iye, S. Kitagawa, K. Ishida, H. Ikeda, S. Kasahara, H. Shishido, T. Shibauchi, Y. Matsuda, and T. Terashima, *Unconventional Superconductivity and Antiferromagnetic Quantum Critical Behavior in the Isovalent-Doped* $BaFe_2(As_{1-x}P_x)_2$, Phys. Rev. Lett. **105**, 107003 (2010).

[24] S. V. Borisenko, V. B. Zabolotnyy, D. V. Evtushinsky, T. K. Kim, I. V. Morozov, A. N. Yaresko, A. A. Kordyuk, G. Behr, A. Vasiliev, R. Follath *et al.*, *Superconductivity without Nesting in LiFeAs*, Phys. Rev. Lett. **105**, 067002 (2010).

[25] K. Umezawa, Y. Li, H. Miao, K. Nakayama, Z.-H. Liu, P. Richard, T. Sato, J. B. He, D.-M. Wang, G. F. Chen *et al.*, *Unconventional Anisotropic s-Wave Superconducting Gaps of the LiFeAs Iron-Pnictide Superconductor*, Phys. Rev. Lett. **108**, 037002 (2012).

[26] S. H. Baek, L. Harnagea, S. Wurmehl, B. Buchner, and H. J. Grafe, *Anomalous Superconducting State in LiFeAs Implied by the* ^{75}As *Knight Shift Measurement*, J. Phys. Condens. Matter **25**, 162204 (2013).

[27] S. Kitagawa, Y. Nakai, T. Iye, K. Ishida, Y. Kamihara, M. Hirano, and H. Hosono, *Stripe Antiferromagnetic Correlations in* $LaFeAsO_{1-x}F_x$ *Probed by* ^{75}As *NMR*, Phys. Rev. B **81**, 212502 (2010).

[28] C. Chu, F. Chen, M. Gooch, A. Guloy, B. Lorenz, B. Lv, K. Sasmal, Z. Tang, J. Tapp, and Y. Xue, *The Synthesis and Characterization of LiFeAs and NaFeAs*, Physica (Amsterdam) **469C**, 326 (2009).

[29] N. Qureshi, P. Steffens, Y. Drees, A. C. Komarek, D. Lamago, Y. Sidis, L. Harnagea, H.-J. Grafe, S. Wurmehl, B. Büchner *et al.*, *Inelastic Neutron-Scattering Measurements of Incommensurate Magnetic Excitations on Superconducting LiFeAs Single Crystals*, Phys. Rev. Lett. **108**, 117001 (2012).

[30] C. C. Homes, M. Reedyk, D. A. Crandles, and T. Timusk, *Technique for Measuring the Reflectance of Irregular, Submillimeter-Sized Samples*, Appl. Opt. **32**, 2976 (1993).

[31] T. Berlijn, C.-H. Lin, W. Garber, and W. Ku, *Do Transition-Metal Substitutions Dope Carriers in Iron-Based Superconductors?*, Phys. Rev. Lett. **108**, 207003 (2012).

[32] M. Neupane, P. Richard, Y.-M. Xu, K. Nakayama, T. Sato, T. Takahashi, A. V. Federov, G. Xu, X. Dai, Z. Fang *et al.*, *Electron-Hole Asymmetry in the Superconductivity of Doped* $BaFe_2As_2$ *Seen via the Rigid Chemical-Potential Shift in Photoemission*, Phys. Rev. B **83**, 094522 (2011).

[33] S. Ideta, T. Yoshida, I. Nishi, A. Fujimori, Y. Kotani, K. Ono, Y. Nakashima, S. Yamaichi, T. Sasagawa, M. Nakajima *et al.*, *Dependence of Carrier Doping on the Impurity Potential in Transition-Metal-Substituted FeAs-Based Superconductors*, Phys. Rev. Lett. **110**, 107007 (2013).